

Farooq, M.U. and Villarrutia, R. and MacLaren, I. and Kungl, H. and Hoffmann, M.J. and Fundenberger, J.-J. and Bouzy, E. (2008) *Using EBSD and TEM-Kikuchi patterns to study local crystallography at the domain boundaries of lead zirconate titanate*. Journal of Microscopy, 230 (3). pp. 445-454. ISSN 0022-2720

<http://eprints.gla.ac.uk/4862/>

Deposited on: 19 January 2009

Using EBSD and TEM-Kikuchi patterns to study local crystallography at the domain boundaries of Lead Zirconate Titanate

M U Farooq¹, R Villaurrutia¹, I MacLaren¹, H Kungl², M J Hoffmann², J-J Funderberger³, E Bouzy³

¹Department of Physics and Astronomy, University of Glasgow, Glasgow G12 8QQ, UK

²IKM, Universität Karlsruhe, Haid-und-Neu-Str. 7, 76131 Karlsruhe, Germany

³LETAM, UMR CNRS 7078, ISGMP Bât. B, Ile du Saulcy, F57045 METZ cedex 1, France

E-mail: i.maclaren@physics.gla.ac.uk

Summary

Reliable EBSD mapping of “90°” domains in a tetragonal ferroelectric perovskite has been achieved for the first time, together with reliable automated orientation determination from TEM-Kikuchi patterns. This has been used to determine misorientation angles at “90°” domain boundaries and thus local c/a ratios. The

sources of orientation noise/error and their effects on the misorientation angle data have been thoroughly analysed and it is found that this gives a cosine distribution of misorientation angles about the mean with a characteristic width related to the width of the orientation noise distribution. In most cases a good agreement is found between local c/a ratios and global measurements by X-ray diffraction, but some clear discrepancies have also been found suggesting that real local variations are present, perhaps as a consequence of compositional inhomogeneities.

1. Introduction

Lead Zirconate Titanate (PZT), $\text{Pb}(\text{Zr}_x\text{Ti}_{1-x})\text{O}_3$, based piezoelectric ceramics are an important class of functional materials and are widely used as sensors, transducers, actuators, multilayer capacitors, and ferroelectric memory devices. Ferroelectric materials develop a spontaneous electrical polarisation below the Curie temperature and this is usually coupled with a crystallographic distortion; this coupling between crystallographic distortion and electrical polarisation leading to the piezoelectric effect. In order to minimise both strain and electrostatic energies, domains are formed in the grains with different polarisation orientations and these normally form boundaries at specific crystallographic planes to minimise strain (Fousek and Janovec, 1969; Sapriel, 1975). PZT ceramics with $x < 52.5\%$ adopt a tetragonally distorted perovskite crystal structure below the Curie temperature and as a consequence of the significant distortion of the unit cell ($> 2\%$) lamellar domain structures are formed with the domain boundaries on stress-free $\{101\}$ planes and the unit cells in the two domains related by a rotation of nearly 90° about a $\langle 010 \rangle$ axis. The exact rotation angle is related to the c/a ratio of the material through the formula:

$$c/a = 1/\tan([90^\circ - \alpha]/2)$$

where α is the deviation from 90° (MacLaren *et al.*, 2005). There have been suspicions in the past that the composition and structure of PZT is not always homogeneous due to processing considerations, and therefore methods for assessing local (sub-micron scale) crystallography are likely to be very useful. This local crystallography can be assessed using orientation mapping in electron microscopy, provided the accuracy of orientation determination is sufficient ($\sim 0.1^\circ$). Though our main focus is to study PZT because of its technological relevance, the present paper concentrates on developing automated methods for accurate and unambiguous indexing of domain orientations in tetragonal perovskite ceramics using both electron backscatter diffraction (EBSD) and transmission electron microscopy (TEM) Kikuchi patterns, assessing the accuracy of such techniques and the effect of errors/noise on the results, and using these to make some initial comparisons of local and bulk crystallography.

2. Experimental procedures

The material for investigation was received in the as-sintered state in the shape of cylinders with a diameter of about 9 mm. The samples for microstructural investigations were prepared by sectioning the pieces vertically as shown in Fig. 1. The thickness of sections cut for TEM and EBSD analysis was 1 and 2 mm, respectively.

Specimens for EBSD were ground on 1000 grit silicon carbide papers and polished using 6, 3 and 1 μm diamond paste, followed by a final polish with colloidal silica to remove strains and provide a high quality surface finish; a light etch of 100 ml H_2O , 5 ml HCl and five drops HF was applied for 11 seconds to reveal a slight amount of domain topography and finally a thin coat of carbon was evaporated onto

the sample to minimise charging. It was unfortunately not possible to measure the thickness of the coating in the carbon coater we use. The coating thickness is assessed by observing change in resistance of a Cu grid, connected to an electric circuit, placed beside the sample in the coating chamber; as the coating thickness increases the resistance of the grid decreases and this can be used to reproducibly apply a coating thickness suitable for non-conducting samples but still allowing good EBSD patterns. The EBSD data was obtained using a FEI Quanta 200F environmental scanning electron microscope (SEM) (FEI, Eindhoven, The Netherlands) equipped with an EDAX Digiview II camera (EDAX-TSL, Draper, Utah, USA) to capture the EBSD patterns. For EBSD pattern acquisition the microscope was operated at 25 kV accelerating voltage and 13 mm working distance with the sample tilted to 74° (the maximum allowable tilt for this microscope) using OIM EBSD data acquisition and data analysis software from EDAX (EDAX-TSL, Draper, Utah, USA). The EBSD system was carefully calibrated at the given working distance before the execution of the experiments.

The starting material for TEM specimens was also the rectangular section shown in Fig. 1. Four smaller disks were cut out from each slice. These were then ground to about 150 µm and then dimpled to a thickness of about 20 µm in the centre. The samples were ion milled in a Gatan PIPS (Gatan Inc., Pleasanton, CA, USA) using 4kV Ar⁺ ions and a 4° incidence angle from top and bottom, and finally coated with a thin film of carbon to minimise charging. The TEM investigations were carried out in a FEI Tecnai T20 TEM (FEI, Eindhoven, The Netherlands) operated at 200 kV equipped with an Olympus-SIS Megaview III CCD camera (Olympus Soft Imaging Solutions GmbH, Münster, Germany) for recording the diffraction patterns, typical spot sizes for the analysis were in the range 25-40 nm. The Kikuchi patterns

were recorded using a convergent beam at a relatively low camera length so that the majority of the pattern is projected onto the CCD whilst using the pointer to blank the primary transmitted beam and allow longer exposures of the diffraction patterns before significant overexposure in the central part occurs. Raw Kikuchi patterns display extreme intensity variations from very bright close to the primary beam to very dim and rather noisy at the edges. In order to convert these patterns to ones in which the lines can be automatically detected and indexed, a procedure previously used by Fundenberger *et al.* (2003) was adapted for this case. Firstly, the intensities were first equalised by mapping them onto a logarithmic scale and then the resulting pattern was filtered using a proprietary DCE (differential contrast enhancement) filter in the AnalySIS software (Olympus Soft Imaging Solutions GmbH, Münster, Germany) in order to enhance the Kikuchi lines and Kikuchi band edges. Crystallographic orientations were then determined from the processed Kikuchi patterns using the Euclid's Phantasies (EP) software (Fundenberger *et al.*, 2003). An example is shown later in this paper of the operation of this procedure.

X-ray diffraction was performed using a Siemens D500 diffractometer with Cu K α radiation using an angular range from 20° to 72.5° and a step size of 0.02°. The diffractograms were obtained from bulk samples, which were polished on 4000 grit silicon carbide paper. Following polishing the samples were heat treated at 500°C for four hours to reduce texture effects. The samples had an average grain size of $\sim 5.5\mu\text{m}$. The lattice parameters used for EBSD data analysis were also obtained from X-ray diffraction experiments.

3. Strategy for the EBSD investigation of PZT ceramic

Due to their non-conducting nature, ceramics are more difficult than metals to investigate using EBSD, especially when the goal is to obtain high-resolution orientation data from fine microstructural details. Orientation mapping an area of less than $1\text{ }\mu\text{m}^2$ is similar to a stationary electron beam. These conditions lead to problems like sample charging, image drift and sample surface contamination under the electron beam making long exposures and large maps almost impossible. Therefore, a strategy had to be devised to minimize these problems as well as to obtain the best quality data. To minimize charging and contamination of area of interest an adjacent area was used to refine the focus. Drift problem was minimised by using smaller beam currents. Further a 4×4 binning of the patterns reduced the acquisition time considerably without compromising the quality of the patterns needed for our work. An accelerating voltage of 25kV was used to reduce the exposure time, which was relatively long due to the low current available in the small spot sizes required for these experiments. Band detection was performed using band centres since the band edges were not sharp enough for this purpose. A convolution mask of 5×5 pixels was used to enhance and identify peaks in the Hough transform of the EBSD patterns.

Results

A secondary electron SEM image in Fig. 2 shows an overall distribution of domains across several grains in a lightly etched PZT sample. The lamellar structure of the domains can be clearly seen across much of the surface, and it is also clear that multiple domain structures occur within each grain. The etching treatment was given to facilitate EBSD investigations because the sample surface in the finely polished state does not reveal any microstructural details making EBSD investigation extremely difficult. The etching also removes a thin layer of material minimising the

effects of mechanical polishing. The degree of topography in Fig. 2 seems a little high for EBSD investigations, but this image was taken with the sample tilted 74° towards the detector therefore the appearance of topography is exaggerated. The effect of this topography was studied carefully and it was observed that it did not affect the quality of the whole pattern. Instead a small portion of the pattern was shadowed, which was minimised by dynamic background subtraction. The orientation maps in Figs. 3a and 3c show a clear delineation of 90° domains according to the inverse polefigure colour key (Fig. 3e). These maps were collected from the domains marked by the polygons in Figs. 3b and 3d respectively. In spite of the high topography in Fig. 3d the orientation of 90° domains could be obtained successfully though the number of misindexings were relatively higher $\sim 5\%$ in this map (Fig. 3c) as compared to $\sim 1\%$ in Fig. 3a. Fig. 4 shows domain boundary maps from different samples. Figs. 4a and 4b are domain boundary maps of the same area as in Figs 3a and 3c while Fig. 4c is from La-Sr doped 37.5% Zr/62.5% Ti. In the maps domain boundaries are highlighted with coloured lines and overlaid on the pattern quality map. The colours represent different angles in the misorientation angle histograms (Fig. 4b, d and f), which present the statistical distributions of the misorientation angles across the domain boundaries. Some of the pixels in the grain boundary map show abrupt colour changes as compared to the adjacent pixels e.g blue and red pixels in the lower end of the domain boundaries in Fig. 4a. Such points occur due to errors in the indexing of the EBSD pattern (perhaps due to poor quality patterns at those points as a result of pattern overlaps at boundaries, surface contamination, surface damage, or similar) and appear in the extreme right and left ends of the misorientation histograms. These values are not included when calculating the mean misorientation value from the data in these histograms. Moreover other random errors are present in all

measurements of crystal orientations for a number of reasons including those related to the sample and those related to the orientation measurement system (Godfrey *et al.*, 2002; Bate *et al.*, 2005). Sample issues may include surface relaxation, sample bending, and surface layers (including deliberate carbon coating) resulting in loss of pattern definition making the lines harder to detect. Measurement errors are believed to be mainly due to diffuseness of the pattern and noise in the CCD camera and its electronics making line location slightly uncertain, also variations in line detection routines can bias the solutions in different directions – a different set of lines detected may result in a slightly different answer. Domain boundary maps have also been obtained from other samples with various compositions and shown with their corresponding histograms in Fig. 4(c-f). Although the mean misorientation is different in each case still the statistical distribution about the mean value is similar proving the reproducibility of the data. Comparing the statistical distribution of misorientation angles obtained from different areas in the same sample has also revealed that the mean value may show small but noticeable variations. As outlined above, the misorientation angle determined for a region, and specifically its deviation from 90° reveals key information about the local crystallography in the form of the local c/a ratio and this data is summarised in Table 1 for EBSD data from three different samples.

For comparison with the EBSD results, misorientations between parallel domains were also obtained from samples investigated in TEM. Fig. 5 shows an example of the automated indexing of a Kikuchi pattern from the TEM. These Kikuchi patterns were indexed using the Euclid's Phantasies (EP) software (Fundenberger *et al.*, 2003). It was found that provided suitable patterns are recorded with sufficient intensity to allow clear band detection to the edges of the image,

unambiguous indexing of the unit cell orientation (not just of the pseudocubic perovskite cell, but also including of the long c -axis direction) was routinely achieved. A raw TEM-Kikuchi pattern with the pointer is shown in Figure 5a, and the processing steps are then outlined in Figure 5b-d. Figure 5b shows the result of flattening the high intensity regions and enhancing the low-intensity regions using a logarithmic display of intensity. Figure 5c then shows the result of applying an edge-enhancing DCE filter to this logarithmic image; all lines and band edges become much better defined and are thus easier to detect automatically, but the enhancement of noise at the corners of the pattern is also noticeable. Finally, after automatic line detection and fitting of a solution, a display like that in Figure 5d is achieved where the predicted Kikuchi lines are overlaid in red on the pattern; a very good match between the experimental pattern and the overlaid solution may be noted. This procedure was used to determine relative orientations at a domain boundary in undoped 50% Zr/50% Ti PZT sample. Fig 6 shows an area of this sample having parallel domains with the sample oriented such that the domain boundaries are almost edge-on; the locations from where the TEM-Kikuchi patterns were obtained in parallel domains are marked with numbers. This image was taken without an objective aperture in the TEM due to technical difficulties on the microscope, resulting in some minor striation contrast in domains 2 and 4, which is not due to presence of nanodomains (Schmitt *et al.*, 2007). Among all the compositions studied in this work only the undoped 50% Zr/50% Ti composition showed any nanodomains at all in TEM studies, and these were very infrequently observed e.g. two nanodomains can be seen at the head of domain 6 near the tip of domain 5. However, nanodomains have not yet been studied in any detail using the methods detailed in this work. The misorientations between adjacent domains are given in Table 2. These

values again show a small variability, and this will be discussed in the next section. The misorientations calculated from this and similar regions from other samples are given in Table 1, converted to equivalent c/a ratios, and compared with EBSD results from the same samples.

In order to provide a comparison with global measurements, c/a ratios were also determined from X-ray diffractograms using simple comparison of the 200 and 002 peak positions with zero point correction; these are also summarised in Table 1.

4. Discussion

It has been shown above in Fig. 4 that the misorientations in EBSD tend to show some variation about an average value with a standard deviation typically in the range $0.1\text{-}0.2^\circ$. The source of this error was investigated further by recording EBSD patterns from a single crystal silicon wafer using an area of $800 \times 400 \text{ nm}^2$ with a step size of 20 nm using the same system settings as for PZT material. Data from within a single domain of PZT was also analysed for its misorientation distribution between adjacent points. The misorientation histograms resulting from these experiments are shown in Figure 7. For the case of silicon the median[†] of the distribution lies at 0.105° , for PZT this lies at 0.165° in this graph, which is possibly the worst case scenario, some other measurements suggest a smaller orientation scatter for PZT. It may be noted that these misorientation distributions can be fitted fairly well by a Rayleigh distribution:

$$A \delta \exp(-\delta^2/B)$$

where A and B are adjustable parameters, and δ is the misorientation due to random errors from sample and measurement system (Godfrey *et al.*, 2002) and this fit is

[†] Using the mean of the distribution skews the measurements to high angle due to the few high angle misorientations

shown on Fig. 7a and 7b. The fit to the Rayleigh distribution is quite good for the Si, which has better statistics, whereas it is a bit more sketchy for the PZT, probably mainly as a result of too few orientations analysed resulting in poor counting statistics. The main conclusion of the slightly wider distribution for PZT as compared to silicon is that we cannot determine misorientations as well for PZT as for Si. One reason for this will be intrinsic to the materials, since electronic interactions will be more likely in the high-Z PZT resulting in more diffuse scattering with significant energy losses leading to the formation of a more blurred Kikuchi pattern (Deal *et al.*, 2007; MacLaren, unpublished data), whereas in the low-Z silicon, phonon interactions resulting in high angle scattering without significant energy loss will be proportionately more likely, resulting in the formation of a sharper Kikuchi pattern. Another reason for the difference may be related to sample preparation since in the case of PZT the carbon film on the surface will probably cause diffuse scattering and reduce the sharpness of the pattern; although there may be some native oxide on the Si surface, the effect is probably less.

Orientation noise also arises in TEM Kikuchi pattern measurements, as a consequence of slight variation in the set of bands detected in a pattern: this may arise as a consequence of contrast, orientation or thickness changes, and sometimes slight changes to the software settings used for band detection are necessary where the standard settings give a match which clearly does not fit some of the outlying lines. Such changes can just have the consequence of finding a crystallographically equivalent solution to the original solution but can also introduce small misorientations. An experiment was performed where the band detection parameters were adjusted slightly to produce 6 different indexings of the same pattern, all of which appeared by eye to fit the bands very well. The misorientations between all of

these orientation determinations were then calculated to give 15 different misorientation values. From these we were able to calculate a mean misorientation angle of 0.09° (or median of 0.08°) with all values $< 0.2^\circ$, suggesting that the instrumental accuracy of orientation determination from TEM-Kikuchi patterns is better than that for EBSD.

The other main source of error in orientation measurements in the TEM will arise from the bending of the thin TEM specimens; this may be measured by recording Kikuchi patterns from different areas within the same domain by simply translating the specimen without tilting, or equivalently, translating the beam without tilting (which requires a carefully aligned microscope). Current measurements suggest that closely separated areas may have misorientations of less than 0.2° , but more widely separated areas often have misorientations of greater than 0.5° ; the situation is especially bad for the thinner areas adjacent to holes in the ion-beam-thinned specimens, probably due to stress relaxation in these very thin areas. This would suggest that the main limitation to accurate misorientation measurement in the TEM arises from sample bending and not from indexing accuracy. To minimise the effect of this bending on the results two steps can be taken: firstly to only work with data from relatively thick areas of the specimen, and secondly to use the smallest possible step size between spots used for the analysis of the relative orientations between features in a sample. TEM investigations of un-doped PZT 50% Zr/50% Ti has shown that in relatively thick TEM samples where stress release and sample bending were minimised, the c/a ratio was found to be more or less the same over large distance (Table 2).

The important question for our work on “ 90° ” domains is how these orientation variations within a single crystal as a result of indexing and specimen

preparation issues affect the misorientation measurements across domain boundaries. Fortunately, the effects of a small misorientation error on a misorientation measurement have already been calculated by Bate *et al.* (2005) and the extension of their analysis to calculating the error in a misorientation angle is given in the Appendix to this paper. The main conclusion of this is that if there is a random misorientation from a measurement error, it will affect the measured misorientation angle in different ways depending on the relative orientation of the real and the random misorientation axes; a random distribution of misorientation axes for a fixed error angle, δ , will give a cosine distribution of angles about the true misorientation but will not shift the centre of the distribution significantly for high misorientation angles. In reality, we do not see just a fixed error angle, δ , but a distribution approximating to a Rayleigh distribution, as previously suggested by (Godfrey *et al.*, 2002) so this Rayleigh distribution will somehow be convoluted with the cosine distribution of errors. Fig. 8 shows a misorientation distribution graph for a 90° domain boundary in the PZT with a cosine distribution fitted to this distribution. The distribution fits extremely well with just some slight tails to the distribution, which probably arise from the tails of the Rayleigh distribution. Thus, the distribution of misorientation angles about the central value is very well approximated by a cosine distribution. Most of the EBSD orientation maps give misorientation angle histograms which can be approximately fitted by a cosine graph, and in many cases the standard deviations on the misorientation angles listed in Table 1 compare well with the expectation of $\delta / \sqrt{\pi} \approx 0.09^\circ$, with some listed errors such as 0.06° , 0.08° , and 0.12° . In other cases, larger errors are seen, and there could be a number of reasons for this including poorer pattern quality due to microscope setup or specimen

preparation related factors, also in one case, it appeared possible that the distribution was bimodal with two different boundaries having slightly different misorientations.

Hence it can be inferred that the statistical distribution of misorientation angles along a domain boundary, as shown in Fig. 4, is caused by orientation noise rather than real crystallographic or compositional variations along a domain boundary. However for the same sample a relative shift of the mean value of statistical distribution of misorientation angles obtained from different sample areas may well indicate that the c/a ratio is not constant throughout the sample. Analysing the results shown in Table 1, it would appear that the c/a ratios indicated for the La-Sr doped samples by both TEM-Kikuchi and EBSD tend to match pretty well to those expected from the bulk XRD measurements, although there are some possible deviations for the 37.5% Zr / 62.5% Ti sample. For the undoped 50% Zr / 50% Ti sample, however, some larger discrepancies may be noted for both TEM-Kikuchi and EBSD measurements. These may well indicate local variations in c/a ratios from the bulk average as a result of local compositional inhomogeneities, but more work will be required to confirm whether or not real compositional and crystallographic heterogeneities are really present in these materials.

It is also clear that if the orientation noise could be reduced, we would have a better chance of unambiguously detecting small changes in local crystallography. At present, the difference between the La-Sr doped 42.5/57.5 and 50/50 samples (c/a nominally 1.0301 and 1.0239) is enough that we have no difficulty in distinguishing these c/a ratios using EBSD or TEM-Kikuchi based methods. To detect smaller changes in composition and thus c/a we would need to have more accurate methods for orientation measurement, especially in EBSD. There are a number of things that can be done in this area. Firstly, improved pattern quality (better signal to noise)

would help, and in this respect a better EBSD camera would be a significant help. Secondly, Bate *et al.* (2005) have shown better accuracy of orientation determination using pattern matching methods rather than Hough transform based methods, and these could be explored in future work. Similarly, care will need to be taken with TEM data to maximise accuracy and thus maximise our chances of being able to detect smaller lattice parameter changes.

5. Conclusions and further outlook

Successful EBSD mapping of 90° domain structures in a perovskite ferroelectric has been demonstrated for the first time. The results also allow us to measure the misorientation angle distribution at these domain boundaries and the deviation from 90° allows us to determine the local c/a ratio. Automated orientation measurement from TEM Kikuchi patterns from such domains in PZT has also been demonstrated for the first time, and comparable results have been achieved. The sources and quantity of orientation scatter or noise in both the EBSD system and the TEM have been considered; in EBSD orientation scatter leads to an uncertainty, δ , of the order of 0.16° in misorientation measurements on PZT. In TEM, the accuracy of individual measurements is generally better ($< 0.1^\circ$) but is limited by sample preparation since samples often relax on thinning resulting in bending and buckling and this can give errors of greater than 0.5° if too widely spaced points are used for analysis. The effects of such random errors on misorientation angle measurements are considered and it is shown that for high misorientation angles this will lead to an approximately cosine distribution of misorientation angles about the mean, with a standard deviation of $\delta / \sqrt{\pi}$, the distribution shape is well reproduced in most cases, and the distribution width matches well to our estimates in some cases, whereas in others higher errors are

found. In general we find that the local c/a ratios are in good agreement with global values measured by X-ray diffraction, but some cases have been found where local values appear to show significant discrepancies from XRD values, such cases will be investigated further in future work to determine whether these are correlated with compositional inhomogeneities.

Acknowledgements

Rene De Kloe from EDAX is gratefully acknowledged for help in developing routines to enable the unambiguous indexing of 90° domain-orientations from EBSD patterns of PZT. This work would have been impossible without the help of Messrs. Peter Chung, Brian Miller, John Gilleece and Colin How and the provision of EBSD time by Dr Martin Lee.

5. References

- Bate, P.S., Knutsen, R.D., Brough, I., and Humphreys, F.J. (2005) The characterization of low-angle boundaries by EBSD. *J. Microsc. (Oxford)*, **220**, 36-46.
- Deal, A, Hooghan, TK, and Eades, A. (2008) Energy-filtered electron backscatter diffraction. *Ultramicroscopy*, **108**, 116-125.
- Fousek, J. and Janovec, C. (1969) The orientation of Domain walls in twinned ferroelectric crystals. *J. Appl. Phys.*, **40**, 135-142.
- Fundenberger, J.J., Morawiec, A., Bouzy, E., and Lecomte, J.S. (2003) Polycrystal orientation maps from TEM. *Ultramicroscopy*, **96**, 127-137.
- Godfrey, A., Wu, G. L., and Liu, Q. (2002) Characterisation of orientation noise during EBSP investigation of deformed samples. *Materials science forum*, **408-412**, 221-226.
- MacLaren, I. (2007) Why are my TEM-Kikuchi and electron backscatter diffraction patterns so fuzzy? – On the mechanisms for blurring of experimental Kikuchi electron diffraction patterns. Submitted to *Ultramicroscopy*.
- MacLaren, I., Schmitt, L.A., Fuess, H., Kungl, H., Hoffmann, and M.J. (2005) Experimental measurement of stress at a 4-domain junction in lead zirconate titanate. *J. Appl. Phys.*, **97**, 094102.
- Sapriel, P. (1975) Domain-wall orientations in ferroelastics. *Physical Review B*, **12**, 5128-5140.
- Schmitt, L.A., Schönau, K.A., Theissmann, R., Fuess, H., Kungl, H., and Hoffmann, M.J., Composition dependence of the domain configuration and size in $\text{Pb}(\text{Zr}_{1-x}\text{Ti}_x)\text{O}_3$ ceramics, *J. Appl. Phys.*, **101**, 074107.

Appendix – the effect of small orientation measurement errors on misorientation angle measurements

Bate *et al.* (2005) have already conveniently presented an argument based on quaternion mathematics for the effect of a small error in misorientation measurement on the measured misorientation axis. This is extended here to the effect of the measurement error on the misorientation angle.

Misorientations may be conveniently represented in a 4-dimensional Cartesian space as a *quaternion*, a unit 4-vector, \mathbf{g} , of the form:

$$\mathbf{g} = \{\cos(\omega/2), \sin(\omega/2)\mathbf{d}\}$$

where ω is the rotation angle and \mathbf{d} the rotation axis.

Following their arguments, the effect of adding a small misorientation resulting from random measurement errors will be to multiply \mathbf{g} by this vector by the misorientation quaternion, ϵ , given by:

$$\epsilon = \{\cos(\delta/2), \sin(\delta/2)\mathbf{h}\}$$

where δ is the rotation angle and \mathbf{h} the rotation axis. This results in a modified misorientation vector:

$$\mathbf{g}' = \{\cos(\delta/2)\cos(\omega/2) - \sin(\delta/2)\sin(\omega/2)\mathbf{d}\cdot\mathbf{h}, \cos(\delta/2)\sin(\omega/2)\mathbf{d} + \sin(\delta/2)\cos(\omega/2)\mathbf{h} + \sin(\delta/2)\sin(\omega/2)\mathbf{k}\}$$

where \mathbf{k} is the unit vector perpendicular to \mathbf{d} and \mathbf{h} (i.e. $\mathbf{d}\times\mathbf{h}/(|\mathbf{d}||\mathbf{h}|)$).

Now we are just interested in the first index since this gives us the modified rotation angle:

$$\cos(\omega'/2) = \cos(\delta/2)\cos(\omega/2) - \sin(\delta/2)\sin(\omega/2)\mathbf{d}\cdot\mathbf{h}$$

There are perhaps three important cases to mention: $\mathbf{d}\cdot\mathbf{h} = 0$, $\mathbf{d}\cdot\mathbf{h} = 1$ and $\mathbf{d}\cdot\mathbf{h} = -1$.

For large ω and small δ , then the first term approximates to $\cos(\omega/2)$, and if $\mathbf{d}\cdot\mathbf{h} = 0$ then $\omega' \approx \omega$. For $\mathbf{d}\cdot\mathbf{h} = 1$ then we are just adding two rotations about the same axis so

$\omega' = \omega + \delta$ and similarly for $\mathbf{d} \cdot \mathbf{h} = -1$, we just have two opposite sense rotations about a common axis so $\omega' = \omega - \delta$. All other values of $\mathbf{d} \cdot \mathbf{h}$ add a proportion of the misorientation angle, δ , to ω according to the angle between \mathbf{d} and \mathbf{h} .

We then need to derive the shape of the distribution of misorientation angles given by the various random orientations of the \mathbf{h} axis with respect to \mathbf{d} . We can imagine that the tip of the \mathbf{h} vector lies on a sphere and makes an angle with \mathbf{d} given by $\cos \theta = \mathbf{d} \cdot \mathbf{h}$. The probability of finding any given θ value will be related to the circumference of the circular section through the sphere described by that particular θ value (see Fig. 9), and this circumference is given by $2\pi \sin \theta$ (i.e. there are far more possible orientations of \mathbf{h} perpendicular to \mathbf{d} than there are parallel to \mathbf{d}). Since θ ranges from 0 for $\mathbf{d} \cdot \mathbf{h} = 1$ to π at $\mathbf{d} \cdot \mathbf{h} = -1$, we can then construct a probability distribution for the effect of a fixed rotation, δ , about a randomly oriented \mathbf{h} axis on the measured misorientation angle, ω' . This is plotted in Fig. 10 and is equivalent to a cos function centred on ω . The standard deviation of this distribution may be determined by evaluating the root mean square of this distribution; the appropriate integral of $\cos^2 \theta$ from 0 to $\pi/2$ gives the result $\frac{1}{2}\sqrt{\pi}$. Since the distribution exists in the range $\pm \delta$ (and not $\pm \pi/2$), then the standard deviation $\sigma = \frac{1}{2}\sqrt{\pi} [\delta / (\pi/2)] = \delta / \sqrt{\pi}$. So to conclude, for high misorientation angles, an error of δ in misorientation measurement introduces a cos distribution with a standard deviation of $\delta / \sqrt{\pi}$ into the calculated misorientation angle.

Figure Captions

Fig. 1. The sampling strategy for EBSD and TEM investigations

Fig. 2. SEM secondary electron image of the domain structure of a 37.5%Zr/62.5%Ti PZT sample after etching.

Fig. 3. (a) EBSD orientation map showing parallel domains in a samples of La-Sr doped 50% Zr/50% Ti PZT, (b) Secondary electron image of the area used for mapping, (c) EBSD orientation map of domains in an undoped 50% Zr/50% Ti PZT (d) Secondary electron image of the area selected for mapping. (e) Inverse polefigure colour key.

Fig. 4. (a,b) EBSD domain boundary map and misorientation angle histogram from La-Sr doped PZT 50% Zr/50% Ti. (c,d) Domain boundary map and misorientation angle histogram from an undoped 50% Zr/50% Ti PZT. (e,f) Domain boundary map and misorientation angle histogram from La-Sr doped 37.5% Zr/62.5% Ti.

Fig. 5. A TEM-Kikuchi pattern from a La-Sr-doped PZT La-Sr doped 50% Zr/50% Ti sample. (a) The raw pattern with no contrast adjustment, it is difficult to see much of the pattern when printed; (b) After mapping the intensities onto a log scale to increase the visibility of the low intensity edge regions; (c) After application of a digital (DCE) filter to enhance the band edges. (d) The same pattern as in (c) with solution lines overlaid.

Fig. 6. Bright field TEM image of domains in un-doped PZT 50% Zr/50% Ti with the locations of TEM-Kikuchi patterns marked.

Fig. 7. (a) Low angle misorientation noise obtained a from single orientation Si wafer compared with Rayleigh distribution curve (continuous line). (b) Low angle misorientation noise obtained from a single domain in a PZT 37.5% Zr/ 62.5% Ti sample compared with a Rayleigh distribution curve (continuous line).

Fig. 8. Misorientation distribution graph for a 90° domain boundary a sample of undoped PZT 50% Zr/50% Ti with a cosine distribution fitted to this distribution.

Fig. 9. All possible orientations of \mathbf{h} with respect to \mathbf{d} describe a sphere of unit radius.

All vectors, \mathbf{h} , which make an angle of θ with respect to \mathbf{d} describe a circle on the surface of this sphere of radius $\sin \theta$.

Fig. 10. The distribution of measured misorientations arising from random small misorientations of angle δ about a randomly oriented axis \mathbf{h} .

Figures

Fig. 1.

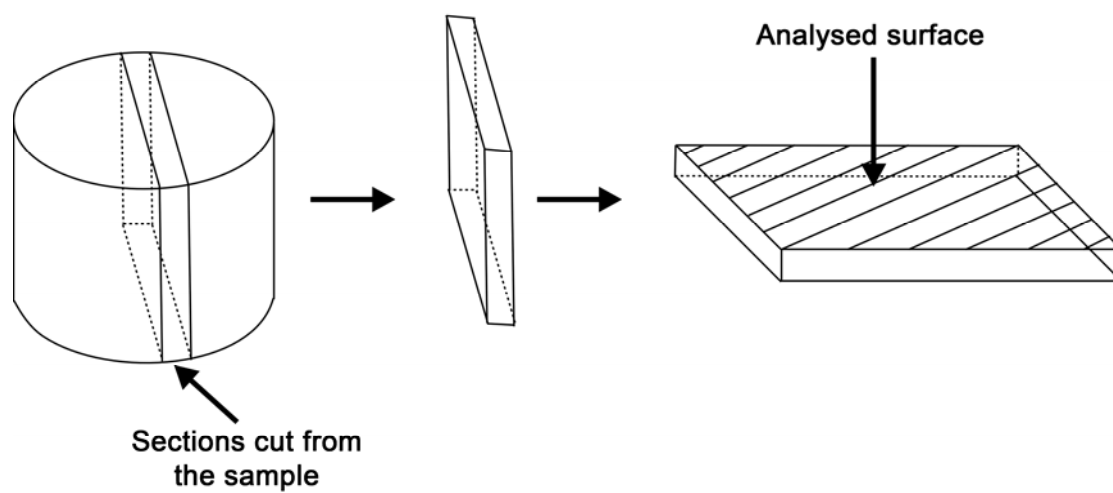


Fig. 2.

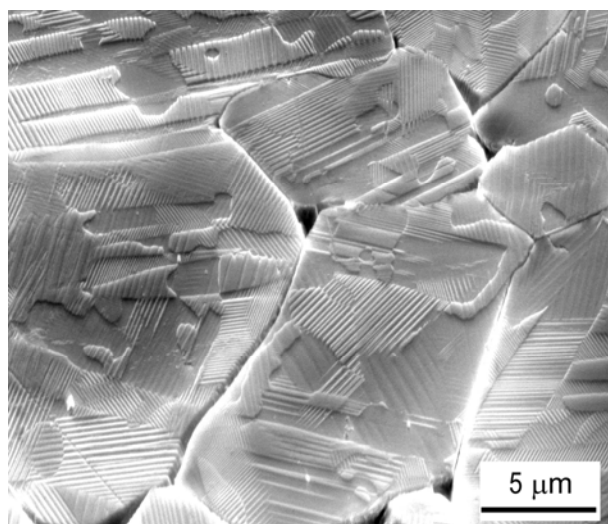


Fig. 3.

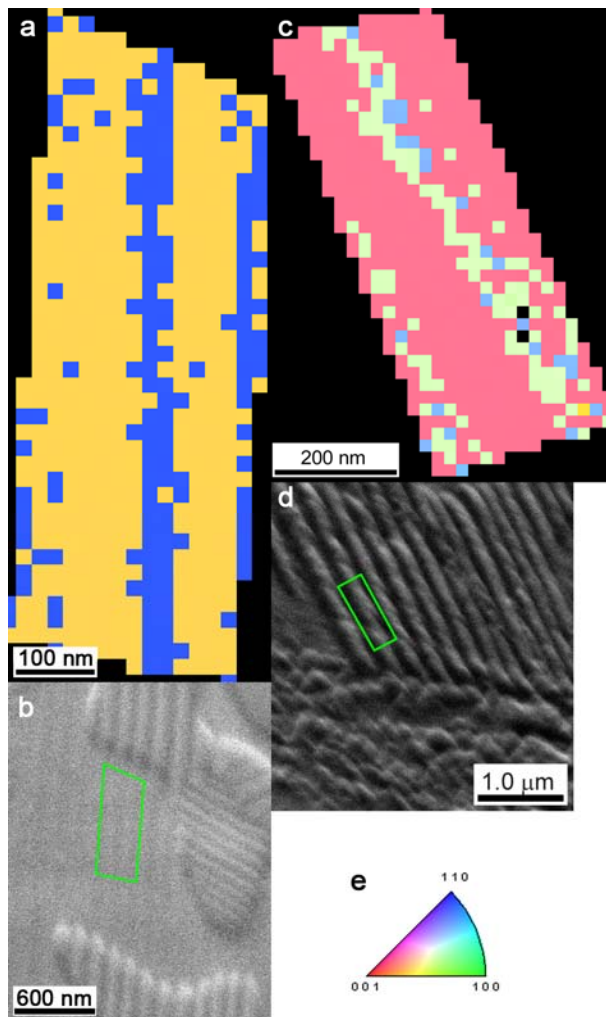


Fig. 4.

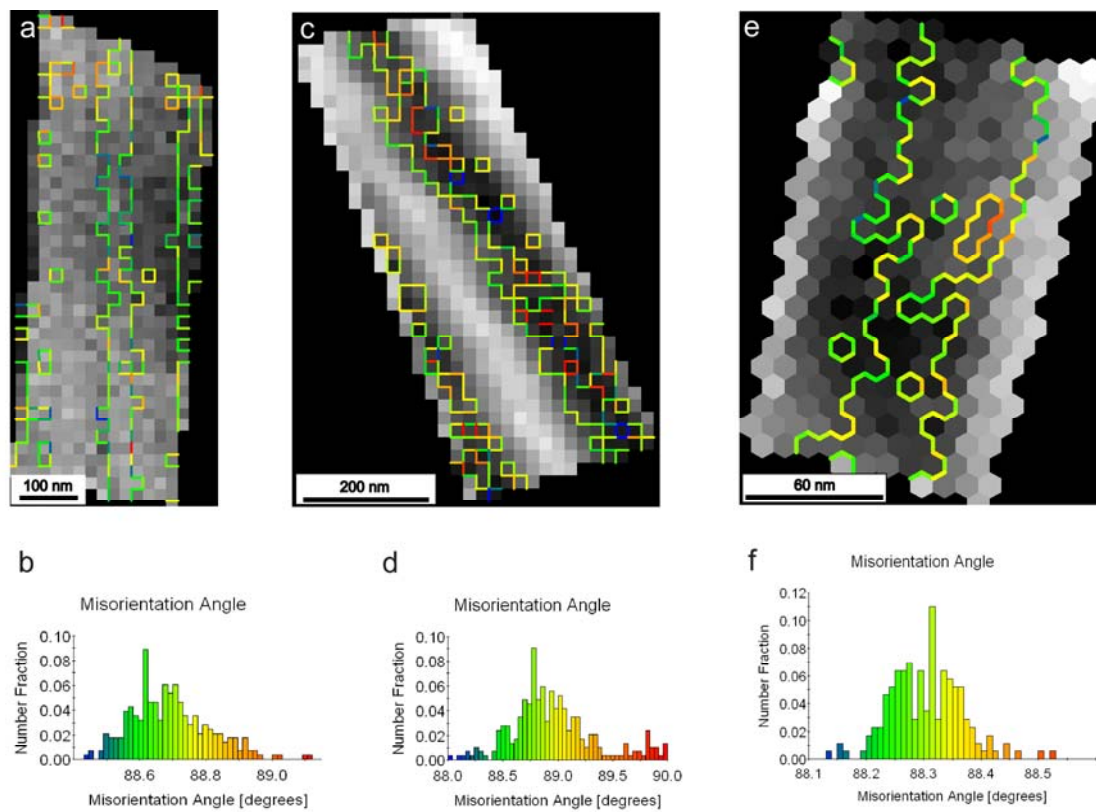


Fig. 5

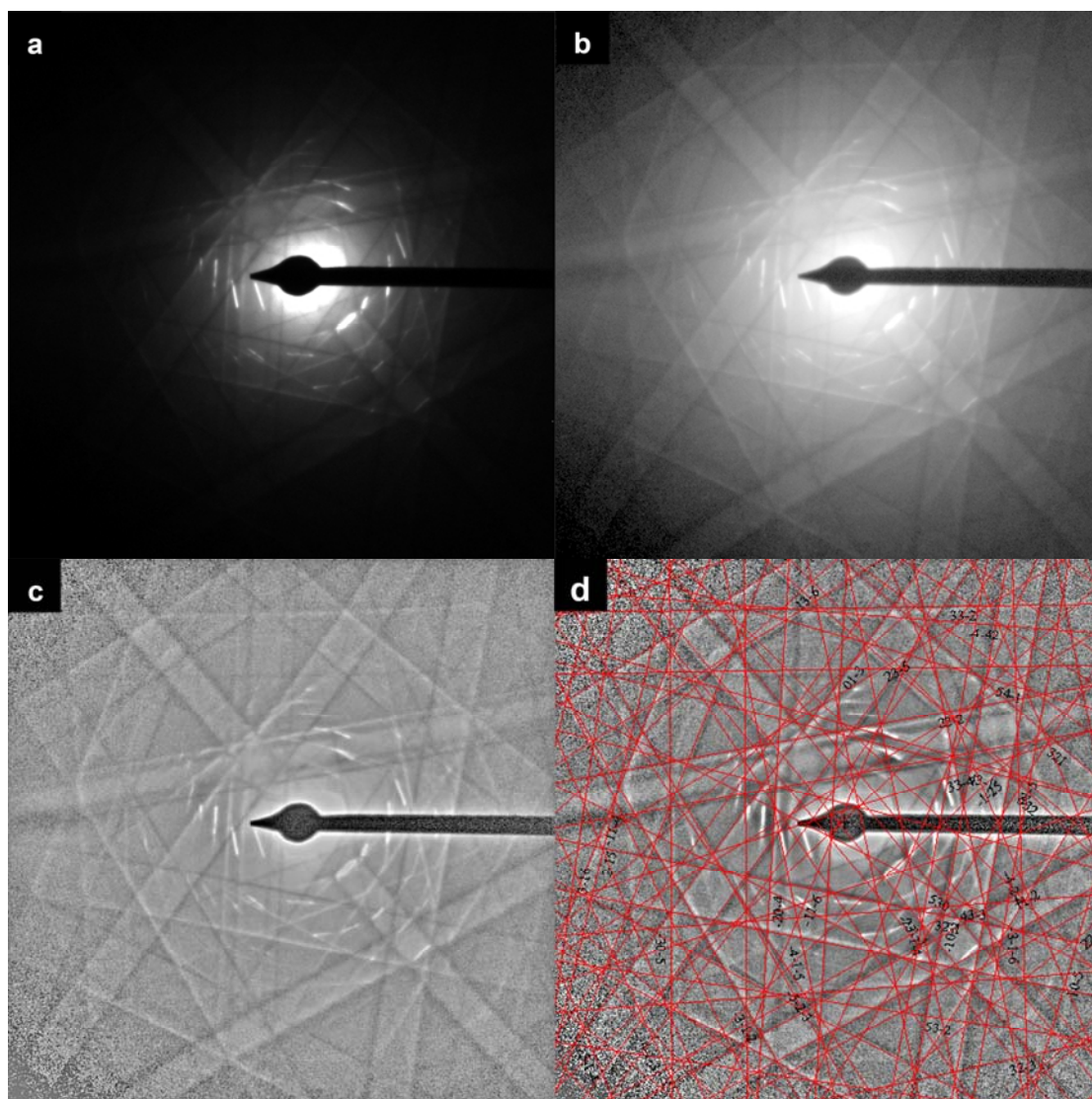


Fig. 6.

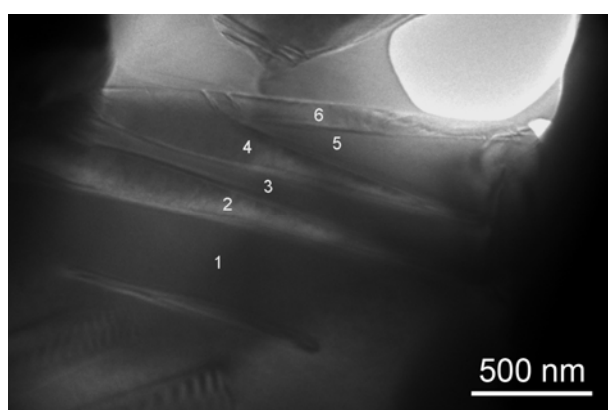


Fig. 7.

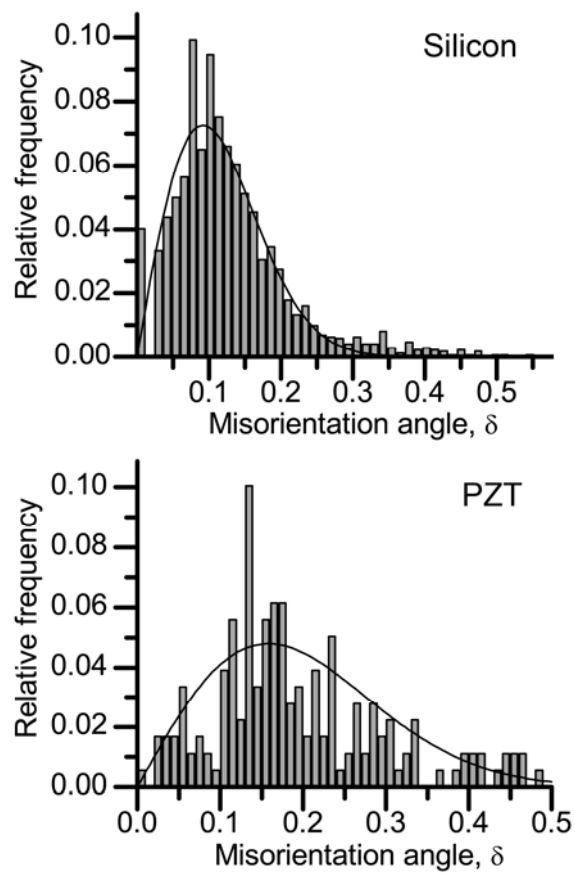


Fig. 8

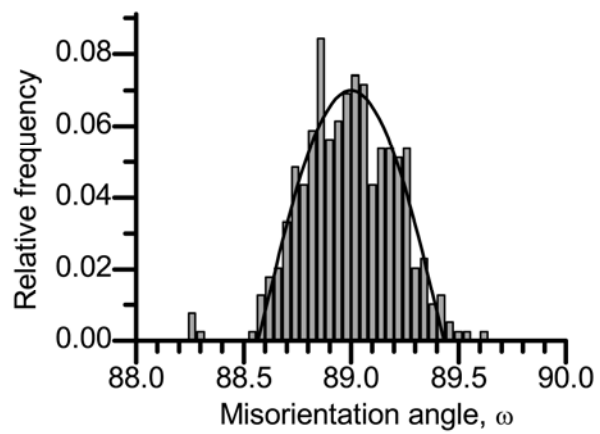


Fig. 9

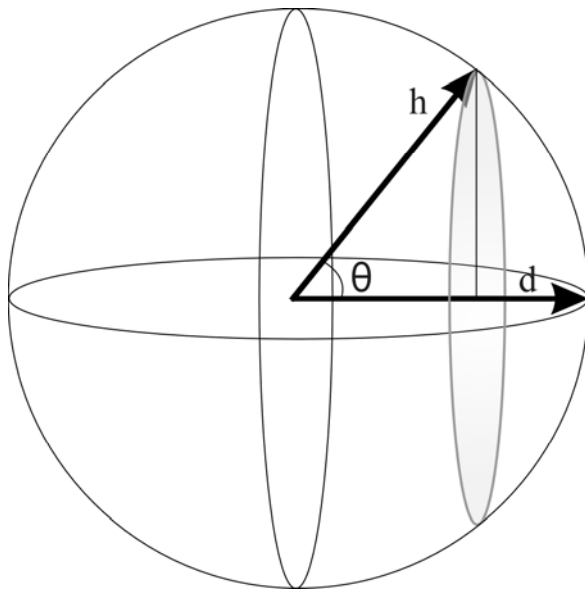


Fig. 10

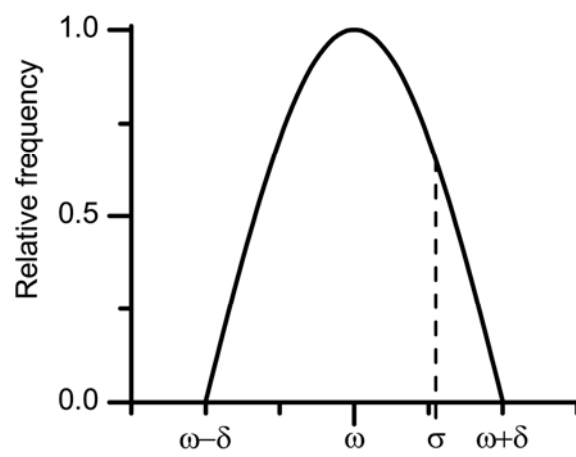


Table Captions

Table 1. Misorientation angles and c/a ratios determined using XRD, EBSD and TEM-Kikuchi pattern methods, where more than one area for the same specimen has been mapped, separate misorientation angle distributions for each area are listed to show variations within a single specimen.

Table 2. Misorientations calculated from the TEM Kikuchi patterns in the regions marked in Fig 6.

Tables

Table 1.

Type of PZT	Composition (%Zr/%Ti)	XRD	TEM - Kikuchi		EBSD	
		c/a ratio	$90^\circ - \alpha$	Local c/a	$90^\circ - \alpha$	Local c/a
La-Sr doped	37.5/62.5	1.034	88.07 ± 0.08	1.034 ± 0.001	88.18 ± 0.23	1.032 ± 0.004
					88.30 ± 0.06	1.030 ± 0.001
					88.31 ± 0.08	1.030 ± 0.002
					88.36 ± 0.34	1.029 ± 0.006
	42.5/57.5	1.030	88.47 ± 0.23	1.027 ± 0.004	88.69 ± 0.12	1.023 ± 0.002
					88.61 ± 0.38	1.024 ± 0.007
Undoped	50/50	1.028	88.29 ± 0.08	1.030 ± 0.001	89.00 ± 0.20	1.018 ± 0.004
					88.89 ± 0.22	1.020 ± 0.004
					89.13 ± 0.12	1.015 ± 0.002

Table 2.

Position pair	1-2	3-4	4-5	5-6
Misorientation ($^\circ$)	88.23	88.32	88.23	88.39
c/a ratio	1.0314	1.0298	1.0314	1.0285